



Copyright Notice

©2012 IEEE. Personal use of this material is permitted. However, permission to reprint/republish this material for advertising or promotional purposes or for creating new collective works for resale or redistribution to servers or lists, or to reuse any copyrighted component of this work in other works must be obtained from the IEEE.

This document was downloaded from Chalmers Publication Library (<http://publications.lib.chalmers.se/>), where it is available in accordance with the IEEE PSPB Operations Manual, amended 19 Nov. 2010, Sec. 8.1.9 (<http://www.ieee.org/documents/opsmanual.pdf>)

(Article begins on next page)

A System for THz Imaging of Low-Contrast Targets using the Born Approximation

Robin Dahlbäck, *Student Member, IEEE*, Tonny Rubæk, Mikael Persson, *Member, IEEE*
and Jan Stake, *Senior Member, IEEE*

Abstract—A THz imaging system, operating at 346 GHz and tailored for implementation of an imaging algorithm based on the Born approximation, is presented. The imaging algorithm provides focusing by compensating for the antenna footprint. This allows for using a more simple antenna system without optical focusing. Several aspects of implementing an imaging algorithm based on the Born approximation in THz imaging are discussed and key system properties are highlighted. The performance of the imaging algorithm is verified by imaging two simple dielectric targets. The results indicate that this approach provides a qualitative indication of the distribution of contrast in the samples complex permittivity and is a potential complement to existing imaging techniques.

Index Terms—Terahertz, THz, sub-millimeter, imaging, Born approximation.

I. INTRODUCTION

IMAGING in the THz spectrum, i.e., from 300 GHz to 3 THz, has received the attention of both industry and an increasing number of research groups in recent years [1], [2]. Research has been conducted in a wide range of disciplines, such as security screening [3], pharmaceutical process control [4] and medical diagnostics [5]. In general, THz imaging systems operate in one of two configurations: Stand-off imaging or sample investigation. Stand-off imaging is used in situations in which it is necessary to be able to observe the target from a distance and covers such applications as security screening [3] and satellite based systems [6].

Sample investigation is characterized by the availability of samples which can easily be brought to the THz imaging system and the permitted time for measurement and signal-processing is often long compared to stand-off system. The main applications for these systems are biomedical diagnostics [7], [8] and material sciences [9], [10]. Common for most systems used for sample investigation is that they employ quasi-optical focusing to produce a focused spot on the sample. As a consequence, a quite complex system of reflectors and lenses needs to be implemented.

For biomedical applications, THz images of tissue samples have been suggested as a possible tool for diagnostics. Imaging can be divided between hard and soft tissue types. For hard

tissue, THz imaging of bone [11], [12] and teeth [13]–[16] has been demonstrated.

Soft tissue types have a high water content and since water is highly attenuating at THz frequencies, the use of THz imaging is in most cases constrained to regions less than a millimeter thick. This also implies that the contrast observed is mainly caused by the differences in water content throughout the sample, with the higher water content resulting in a higher attenuation.

In cancer diagnostics, it has been shown that it is possible to distinguish between healthy and cancerous tissue in excised samples of basal cell carcinoma (skin cancer) [17]–[20], different types of breast cancer [21]–[25], and other types of cancer [26]. THz imaging for wound monitoring has also been demonstrated [27], [28]. A number of other applications, in which the hydration level of the tissue is an indication of physiological condition, e.g., cornea investigation [29], [30], have also been tested.

At Chalmers University of Technology, a THz imaging system for investigation of soft-tissue samples is currently being developed [31]–[33]. In this system, the focusing is performed in the signal processing, thereby eliminating the need for a large and complicated array of reflectors and lenses for focusing. The imaging algorithm used in this system is based on the first-order Born approximation [34] and the antennas are simple open-ended waveguide probes. Different types of advanced imaging algorithms have previously been suggested for THz imaging systems, e.g., diffraction tomography [35], [36] optical coherence tomography [37], CT-inspired systems [38], [39], and methods inspired by synthetic aperture radar (SAR) [40], but these have all been based on the assumption of the antennas being either point sources or the target being so far from the antennas that a plane-wave approximation is suitable. In the present system, the actual antenna patterns are taken into account in order to reconstruct the images.

The first-order Born approximation provides a linear expression for the scattered field resulting from low-contrast scatterers and has previously been applied with success at microwave frequencies, e.g., for ground penetrating radar [41], [42]. The use of the Born approximation is motivated by the fact that most of the published soft-tissue applications have shown only a low to moderate contrast between the different tissue types. As an example, in [5], the authors found that the complex relative permittivity of healthy breast tissue is approximately $3.0 - j4.0$ at 500 GHz while the corresponding value for breast-cancer tissue is approximately $3.5 - j5.7$.

R. Dahlbäck and J. Stake are with the Terahertz and Millimetre Wave Laboratory, Department of Microtechnology and Nanoscience.

T. Rubæk and M. Persson are with the Division of Signal Processing and Biomedical Engineering, Department of Signals and Systems.

Chalmers University of Technology, Göteborg, SE-41296, Sweden, e-mail: dahlback@chalmers.se.

This work was supported by The Swedish Foundation for Strategic Research.

In [20], the properties of skin and basal cell carcinoma (a certain type of skin cancer) were examined, and the complex permittivity found to be approximately $3.7 - j4.6$ for healthy skin tissue and $3.4 - j5.6$ for basal cell carcinoma. With these relatively low contrasts between the healthy and cancerous tissue, the Born approximation is expected to yield satisfactory results.

The imaging system presented here is based on an electronic system topology and is designed for operation at a single frequency. Common ways to implement such systems can be found in [43], [44]. It is composed of mostly in-house manufactured sub-millimeter wave components combined with a custom assembled IF back-end. Measurements are done at a single frequency and long term stability is crucial since the imaging algorithm is sensitive to phase and amplitude drift.

This paper is organized as follows: In Section II, an overview of the system setup is given, which is followed by a detailed description of the electronics in Section III. The antenna configuration, sample holder design, and mechanical scanning are described in Section IV while the imaging algorithm is presented in Section V. Finally, in Section VI, the performance of the system is illustrated using a Mylar target and a leaf.

II. OVERALL SYSTEM SETUP

The system consists of an IF back end and two high-frequency front-end modules, one for the receiver and one for the transmitter. The transmitter front-end consists of the antenna, a broadband Schottky doubler, an HBV varactor quintupler along with an isolator and a coaxial to waveguide transition. The receiver front-end shares its configuration with the transmitter with the exception of the doubler which is replaced by a second harmonic Schottky mixer [45].

A photograph of the entire measurement setup is shown in Figure 1, a close-up of the measurement region in Figure 2, and a block diagram of the measurement hardware is shown in Figure 3. The IF system creates both the transmit signal and the LO-drive signal for the receive side. The two signals are offset by $1/10$ of the first IF frequency by the use of a frequency divider and thus also phase correlated to reduce measurement noise [46]. The first IF frequency, from the output of the sub-harmonic mixer, is then down-converted by an I/Q-demodulator to an I and Q DC signal which is amplified and finally detected in the data acquisition system.

The system operates by measuring the amplitude and phase of the 346 GHz signal after transmission through the sample. Both antennas are open-ended waveguides and mounted on separate mechanical stages, allowing them to move independently in two parallel planes.

III. MEASUREMENT HARDWARE

A common approach for realizing CW THz systems is up-conversion from microwave frequencies using frequency multipliers for signal generation and sub-harmonic mixers for detection [47], [48]. This approach is also applied in this system and the system electronics can be divided into two parts; the IF back-end where signals are generated and received

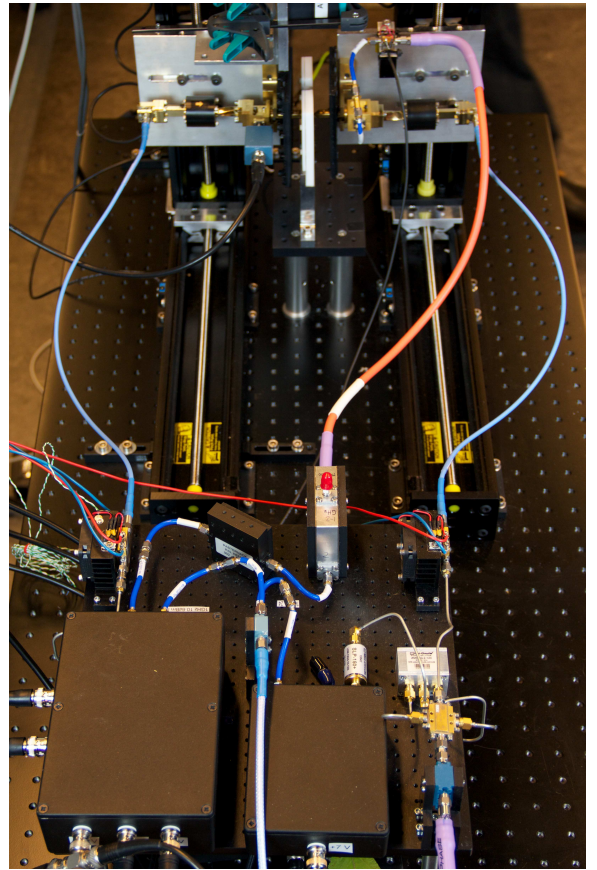


Fig. 1. A photograph of the measurement system. The IF back-end is located on the optical breadboard in the lower part of the picture. In the upper part of the picture, the measurement region is shown, see close-up in Figure 2.

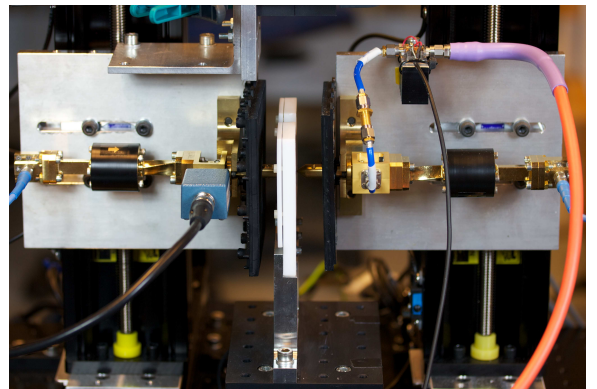


Fig. 2. A photograph of the high-frequency modules and the measurement region. The transmitter module is on the left and the receiver on the right. The white frame in the middle is the sample holder.

and the high-frequency front-end consisting of frequency multipliers and a sub-harmonic mixer. Two CW sources drive the system, one high-frequency synthesizer operating at 34.6 GHz and one low-frequency synthesizer operating at 912 MHz.

A. IF back-end

The IF back end, indicated by the lower dashed box in Figure 3, is constructed around easily available and inexpensive commercial communication components.

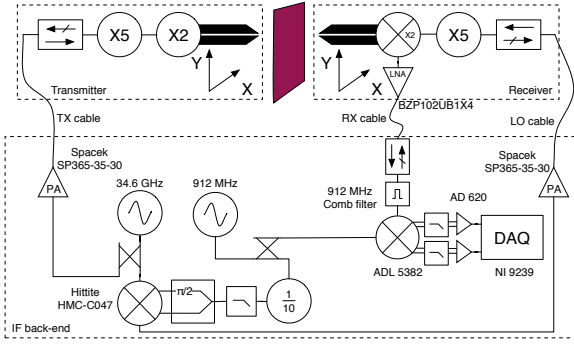


Fig. 3. Block diagram showing the electronics, the if back-end is connected to the high-frequency parts by flexible cables (shown as curled).

Starting at the high-frequency synthesizer, which operate at one tenth of the measurement frequency, the signal is split in two. One part is fed directly to a PA (Spacek SP365-35-30) which drives the transmitter high-frequency chain and the other part is fed as LO to an I/Q mixer (Hittite HMC-C047).

The output from the IF reference synthesizer, operating at 912 MHz, is also split in two with one part fed to an in-house manufactured 1/10 frequency divider. The 91.2 MHz output signal of the divider is low-pass filtered (Mini-circuits SLP-150+) and then up-converted to the lower sideband of the 34.6 GHz signal through the $\pi/2$ phase-splitter (Mini-Circuits ZMSCQ-2-120) and I/Q-mixer (Hittite HMC-C047). The output from the single-sideband modulator is then amplified in a PA (Spacek SP365-35-30) and fed to the high-frequency receiver chain. Since both the transmitter and the receiver chain have a multiplication factor of ten, the transmit frequency will be 346 GHz and the effective LO frequency of the down-converting mixer will be 345.088 GHz, yielding an IF output frequency from the sub-harmonic mixer of 912 MHz. After amplification in an LNA (B&Z BZP102UBX4), the signal is band-pass filtered around the operational frequency to suppress unwanted spurs.

Since the measured signal has the same frequency and is phase correlated to the reference oscillator, the output from the I/Q demodulator (ADL 5382) will be two DC signals, corresponding to the real and imaginary part of the measured signal. This heterodyne technique allows an amplitude/phase change caused by the object under investigation to be directly measured using the two DC outputs. After amplification (AD620) and filtering, the two DC vectors are digitalized by a 24-bit DAQ (NI 9239).

B. High-frequency front-end

The transmitter outputs approximately 0.5 mW at 346 GHz. The output bandwidth is limited by the varactor-mode multiplier and can be tuned in the region 330-380 GHz. The transmit chain consists of a heterostructure barrier varactor, HBV, quintupler (WASA) [49] and a varistor Schottky doubler (VDI WR-2.8x). The Schottky doubler is a commercial product while the HBV quintupler is manufactured in-house. In addition to the frequency multipliers, an isolator and a coax-to-waveguide transition is used to connect to the IF back-end.

A second-harmonic Schottky mixer, described in [45], is used to down-convert the 346 GHz measurement signal to 912 MHz. The LO drive is provided by an HBV quintupler identical to the one used in the transmit chain. This gives a compact, high performance receiver module.

IV. ANTENNAS AND SAMPLE HOLDER

Two identical antennas and one sample holder, all machined in-house, are used in the system. A photograph of one the antennas is shown in Figure 4 and the plastic sample-holder is shown in Figure 2.

A. Antennas

Two main concerns were addressed during the construction of the antennas and sample holder: standing waves and accuracy of modeling. In the type of setup used here standing waves between different parts of the system pose a severe problem for accurate measurements. Therefore, great care must be taken in the design of all components in the proximity of the measurement region. The antennas are required to be mechanically stable while at the same time giving rise to a minimum of standing waves in the system. This has led to the conical design seen in Figure 4, in which the sloped front deflects incoming electromagnetic fields.

The antennas also need to be simple to model accurately. The reason for the modeling constrain is that the entire measurement area including both antennas and the sample in the sample holder must be included in the same EM simulation. The open ended waveguide fits this purpose since it is simple in construction and has a broad beam.

The sample holder is constructed from a non-conducting machine plastic (PTFE) in order to not introduce large metallic objects in the measurement region. Two pieces of standard 50 by 75 mm sample glass with a thickness of approximately 0.99 mm (Corning Soda Lime Glass 0215), intended for optical microscopy, fixes the sample to the measurement position. To further reduce reflections in the setup, absorbers were mounted on the base of the antennas to dampen waves originating from the antenna mounting structure and the sample holder and glass.

Since the antennas have a broad beam the maximum coupling is as low as -20 dB, when the antennas are positioned in front of each other with two pieces of sample glass in between. This situation is illustrated, with the addition of a Mylar target, in Figure 5.

B. Mechanical positioning and alignment

In order to obtain measurement data from multiple antenna positions, a four-axis mechanical stage is used. The layout consists of two x-y stages, composed of totally four linear slides with lead screw drives (Velmex BiSlide), enabling the transmitter and receiver to move independently in two parallel planes. Measurement data can be collected from arbitrary antenna positions, within the two planes of movement.

The absolute positioning accuracy is important, since the imaging algorithm assumes the positions of the antennas are



Fig. 4. Photograph showing one of the custom built antennas, notice the conical front face and the open ended waveguide aperture. The fine spacing of the ruler is 1 mm.

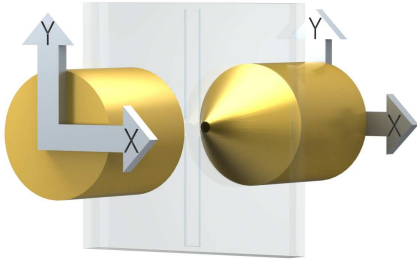


Fig. 5. Antennas, sample and sample glasses, the X-Y arrows indicate the antennas planes of movement.

known. The specified positioning accuracy of the linear slides is $4 \mu\text{m}$ and the straight-line accuracy is specified to $76 \mu\text{m}$ along the entire travel distance. The accuracy of the alignment has been verified across the typical measurement area, approx. 20 by 20 mm.

The exact position of the sample-holder is the only mechanical parameter that changes slightly between measurements, due to the fact that the holder is removed and reassembled with a different sample. A laser profile measurement scanner (Acuity AP620-35C) is used to accurately determine the position of the sample-holder in relation to the two antennas prior to each measurement. The scanner is shown at the top of Figure 1. This procedure is necessary in order to update the EM model for every mounted sample.

V. IMAGING ALGORITHM

As mentioned in the Introduction, an imaging algorithm based on the first-order Born approximation is used for processing the images in the system. The aim of using this algorithm is twofold: First, the algorithm should compensate for the relatively broad beam of the open-ended waveguide antennas. Second, the algorithm should provide information of the complex permittivity of the sample under investigation.

A. Scatter Signal

To formulate our imaging algorithm, it is necessary to derive an expression for the signal change caused by a scattering object in our system. To this end, it is useful to start by

observing the electric field. The total electric field, \mathbf{E}_{tot} , at a given point \mathbf{r} can be written as the sum of the incident field, \mathbf{E}_{inc} , and the scattered field, \mathbf{E}_{sct} , that is,

$$\mathbf{E}_{\text{tot}}(\mathbf{r}) = \mathbf{E}_{\text{inc}}(\mathbf{r}) + \mathbf{E}_{\text{sct}}(\mathbf{r}). \quad (1)$$

The incident field is the field in the system when there is no scatterer present in the imaging domain while the scattered field is the perturbation of the total field caused by the presence of a scatterer in the system. The imaging domain is the region of the imaging system in which the sample is positioned, i.e., the volume between the two glass plates in the sample holder.

Using the volume integral equation [34] and the time notation $e^{j\omega t}$, the scattered field can be expressed as a function of the contrast function O using

$$\mathbf{E}_{\text{sct}}(\mathbf{r}) = j\omega\mu_0 \int_V \bar{\bar{\mathbf{G}}}(\mathbf{r}, \mathbf{r}') \cdot \mathbf{E}_{\text{tot}}(\mathbf{r}') O(\mathbf{r}') d\mathbf{r}'. \quad (2)$$

In this expression, j is the imaginary unit, $\bar{\bar{\mathbf{G}}}$ is the dyadic Green's function [50] and O is the object function [34] given by

$$O(\mathbf{r}) = j\omega (\Delta\epsilon(\mathbf{r})) = j\omega (\epsilon(\mathbf{r}) - \epsilon_{\text{bg}}). \quad (3a)$$

Here, ϵ is the complex permittivity

$$\epsilon = \epsilon' - j\frac{\sigma}{\omega} \quad (3b)$$

with ϵ' and σ being the real-valued permittivity and the effective conductivity, respectively. Subscript bg indicates the known background values. Hence, O is the scaled contrast of the complex permittivity and the expressions in (1) through (3) provide an expression for how the electric field at the antennas change when a scattering object is positioned in the imaging system. The aim of using an imaging algorithm is to extract the distribution of O throughout the imaging domain.

Since the system does not measure the electric field, but rather returns the I and Q voltages measured by the DAQ on the output of the IQ mixer, it is not possible to use the expressions in (1) through (3) directly. Instead, the expressions must be rewritten in terms of the measured signals. To achieve this, the measured signal is written as

$$S_{\text{tot}}(\mathbf{r}_{\text{rec}}, \mathbf{r}_{\text{trans}}) = S_{\text{inc}}(\mathbf{r}_{\text{rec}}, \mathbf{r}_{\text{trans}}) + S_{\text{sct}}(\mathbf{r}_{\text{rec}}, \mathbf{r}_{\text{trans}}). \quad (4)$$

In this expression, S_{tot} is the total signal, S_{inc} is the incident signal and originates from the incident field, i.e., it is the signal measured with an empty imaging system. Similarly, S_{sct} is denoted the scatter signal and is the part of the total signal which originates from the scattered field. The two position vectors \mathbf{r}_{rec} and $\mathbf{r}_{\text{trans}}$ indicate the positions of the receive and transmit antennas, respectively.

The scatter signal can be expressed in terms of the object function O as

$$S_{\text{sct}}(\mathbf{r}_{\text{rec}}, \mathbf{r}_{\text{trans}}) = \alpha \int_V \mathbf{E}_{\text{inc}}^{\text{rec}}(\mathbf{r}', \mathbf{r}_{\text{rec}}) \cdot \mathbf{E}_{\text{tot}}^{\text{trans}}(\mathbf{r}', \mathbf{r}_{\text{trans}}) O(\mathbf{r}') d\mathbf{r}'. \quad (5)$$

Herein, $\mathbf{E}^{\text{trans}}$ is the field in the imaging system when the transmitting antenna is transmitting while \mathbf{E}^{rec} is the field which would be present in the system if the receiving antenna was acting as a transmitter.

The complex scalar α is a system-dependent variable which, among other things, are dependent on the electrical length from the antenna to the DAQ and the attenuation and amplification in the system.

For a rectangular waveguide operating only with the TE₁₀ mode, the value of α can be found by applying the reciprocity theorem. This approach has previously been applied in [51] and [52] for systems being fed through coaxial lines. Under the assumption of the signal S being the commonly applied S-parameter, i.e., the ratio between the output from the receiving antenna and the input on the transmitting antenna, the following expression holds for α_{WG}

$$\alpha_{\text{WG}} = \frac{-Z_{\text{TE}}}{A_{10}^{\text{rec}} A_{10}^{\text{trans}} ab}. \quad (6)$$

In this expression, Z_{TE} is the wave impedance of the waveguide for the TE₁₀-mode and a and b are the length of the long and short side of the rectangular waveguide, respectively. The quantities A_{10}^{rec} and A_{10}^{trans} are the amplitudes of the incident electric field in the waveguide which results in the fields $\mathbf{E}^{\text{trans}}$ and \mathbf{E}^{rec} in (5), respectively.

B. Linear Inversion based on the Born Approximation

The expressions given in (4), (5), and (6) provide an expression for the total measured signal as a function of the object function O . However, because the total field $\mathbf{E}_{\text{tot}}^{\text{trans}}$ is in itself a function of the object function, the inverse problem to be solved for determining the object function is nonlinear. Solving such a problem is a non-trivial and computationally expensive task.

Instead of solving the nonlinear inverse problem, however, it is possible to reformulate the problem. For low-contrast targets, the value of O is low and hence the scattered field is weak compared to the incident field. This implies that the total field in the imaging domain is approximately the same as the incident field, i.e.,

$$\mathbf{E}_{\text{tot}}^{\text{trans}} \approx \mathbf{E}_{\text{inc}}^{\text{trans}}. \quad (7)$$

This simplification is known as the first-order Born approximation [34] and by applying it, the following expression is obtained for the relation between the measured signals and the object function

$$\begin{aligned} S_{\text{tot}}(\mathbf{r}_{\text{rec}}, \mathbf{r}_{\text{trans}}) - S_{\text{inc}}(\mathbf{r}_{\text{rec}}, \mathbf{r}_{\text{trans}}) \\ = \alpha \int_V \mathbf{E}_{\text{inc}}^{\text{rec}}(\mathbf{r}', \mathbf{r}_{\text{rec}}) \cdot \mathbf{E}_{\text{inc}}^{\text{trans}}(\mathbf{r}', \mathbf{r}_{\text{trans}}) O(\mathbf{r}') d\mathbf{r}'. \end{aligned} \quad (8)$$

Since neither of the incident fields in this expression depend on the object function, the inverse problem of determining O is now a linear problem.

The positions of the antennas, as well as the geometry of the empty imaging system, are known which implies that the incident fields from the transmitting and receiving antennas in (8) can be calculated with an EM solver. When doing this, only the waveguide structure of the system is modeled and the

measured signals must therefore be calibrated to be used with the calculated fields. The calibrated signal S_{cali} is given as

$$S_{\text{cali}} = (S_{\text{tot}} - S_{\text{inc}}) \frac{S_{\text{empty}}^{\text{calc}}}{S_{\text{inc}}} \quad (9)$$

where $S_{\text{empty}}^{\text{calc}}$ is the calculated S parameters for the empty system, corresponding to the calculated value of S_{inc} normalized with the input to the transmitting antenna.

The final step in the derivation of the imaging algorithm concerns the discretization of the imaging problem. This discretization is performed by dividing the imaging domain into N_{voxel} voxels in which the object function is assumed to be constant. Hence, the values of the object function may be expressed as

$$O(\mathbf{r}) = O_n \quad \text{for } \mathbf{r} \in V_n \quad (10)$$

with V_n being the volume covered by voxel n . The measurements are performed with the transmitter and receiver positioned at a number, M_{meas} , of discrete positions and thus does not require an explicit discretization.

By combining (8) and (9), a set of linear equations can be created and used to set up the matrix equation

$$\underline{\underline{C}} \mathbf{O} = \mathbf{S}_{\text{cali}}. \quad (11)$$

In this expression, \mathbf{S}_{cali} is a column vector holding the M_{meas} calibrated measured signals and \mathbf{O} is a column vector holding the N_{voxel} unknown discrete values of the object function. The matrix $\underline{\underline{C}}$ has M_{meas} rows and N_{voxel} columns whose elements are given by

$$C_{m,n} = \alpha_{\text{WG}} \int_{V_n} \mathbf{E}_{\text{inc}}^{\text{rec}}(\mathbf{r}', \mathbf{r}_{\text{rec},m}) \cdot \mathbf{E}_{\text{inc}}^{\text{trans}}(\mathbf{r}', \mathbf{r}_{\text{trans},m}) d\mathbf{r}' \quad (12)$$

where $\mathbf{r}_{\text{rec},m}$ and $\mathbf{r}_{\text{trans},m}$ are the positions of the receiving and transmitting antennas, respectively, for measurement m .

From (8), it is clear that the measured scatter signal is a convolution of the contrast in complex permittivity with a kernel consisting of the product of the two fields $\mathbf{E}_{\text{inc}}^{\text{rec}}$ and $\mathbf{E}_{\text{inc}}^{\text{trans}}$. Hence, the imaging algorithm can be seen as a deconvolution operation in which we seek to reconstruct the finer details of O , which are not visible in the raw measurement data. The deconvolution consists of solving (11) for the unknown vector \mathbf{O} . Solving this problem is made difficult by the fact that the problem is ill-posed and underdetermined since the number of voxels in the imaging domain is often much greater than the number of measurement points. This can, of course, be remedied to some extent by choosing fewer voxels in the imaging domain and by increasing the number of measurements.

To solve the problem, the iterative conjugated gradient least squares (CGLS) algorithm [53, Sec. 6.3] is applied and the number of iterations used in the algorithm is determined by applying the L-curve criterion [53, Sec. 4.6]. The most time-consuming part of the imaging algorithm is the calculation of the incident fields which takes several hours. Assembling the coefficient matrix $\underline{\underline{C}}$ and solving the linear problem (11), on the other hand, takes no more than a couple of minutes.

VI. RESULTS AND DISCUSSION

In this section, a number of results will be presented and discussed. These are centered on noise and stability measurements performed with the system, as well as examples of images created with the system.

A. Noise and Stability of the THz Imaging Hardware

The noise performance of the system has been measured using a standard Y-factor measurement approach. To this end, a liquid-nitrogen and a room-temperature load was quasi-optically coupled to the receiving mixer through a corrugated horn. The room-temperature load is constructed as an absorbing chopper and is also used to switch between the hot and cold load. Since the final IQ mixer adds a DC-offset term to the recorded signal it was excluded from the measurement setup during noise measurements. Instead, a power meter was connected to the IF comb-line band-pass filter and an additional LNA was connected to adjust the power level to the range of the meter. Since the original LNA, still attached directly after the mixer, has an amplification of approximately 30 dB, the effect on the measured noise temperature from the addition of an extra LNA is negligible. A Y-factor of 0.34 dB was measured corresponding to a receiver DSB noise temperature of approximately 2600 K. The LNA noise temperature was measured to approximately 100 K and an estimated mixer conversion loss of 10 dB yields a mixer noise temperature of approximately 2100 K DSB.

The overall noise performance of the system provides a dynamic range of 45 dB, which is adequate for imaging of the targets used in this paper.

Since the imaging algorithm is sensitive to system drift, a five hour long stability measurement was performed with the receive and transmit antennas placed opposite of each other and two pieces of sample glass in the sample holder. The result from the five hour long measurement is presented in Figure 6. The total phase variation is in the order of approximately three degrees with a slow negative drift during the measurement. The amplitude is varying within approximately 0.1 dB, with a periodicity of 40 minutes and no noticeable drift during the measurement. The slow oscillation is believed to originate from some slow thermal cycle in either the bias supplies or one of the synthesizers. Overall the stability of the measurement system is very good.

B. Imaging Examples

A number of different targets have been imaged with the system and processed with the proposed imaging algorithm. In this paper, images of two different targets will be presented. One consists of a Mylar sheet in which a cross has been cut while the other consists of a leaf.

The Mylar-sheet target has been chosen since it provides two well-defined uniform regions; the Mylar sheet and the air in the cut. Mylar sheets have previously been applied for tests by other others, both for validation of measurements and for fabrication of meta materials and has a reported relative permittivity of approximately 2.8 at 346 GHz [54], [55].

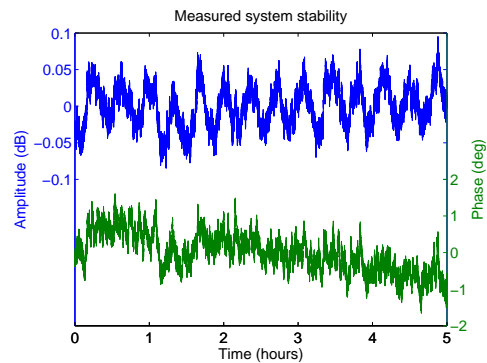


Fig. 6. The amplitude and phase deviation from the mean value during a five hour long stability measurement with the probes stationed opposite each other. The top curve shows the output signal variation from the mean value as a function of time. The lower curve represents the phase behavior of the same signal.

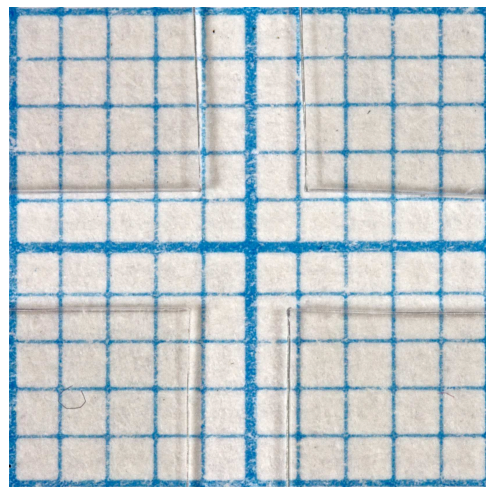


Fig. 7. Photo of the Mylar target. The grid below the target has a line spacing of 1 mm.

The Mylar target consists of 0.12 mm thick Mylar sheet in which a cross has been cut with a scalpel. A photo of the target is shown in Figure 7.

Data was acquired by scanning the transmitter and receiver across an area measuring 10 mm by 10 mm in steps of 0.2 mm. For each transmitter position, one receiver position was used, that is, the receiver was kept directly in front of the transmitter throughout the scan.

For the image processing, the incident fields were calculated using a model consisting of a full model of the antennas, two sheets of glass with a real-valued relative permittivity of 4, and a sheet of Mylar with a real-valued relative permittivity of 2.8. The commercially available EM simulation software CST Microwave Studio was used to calculate the incident fields.

The imaging domain, i.e., the volume filled by the Mylar sheets, was discretized into voxels measuring 0.1 mm in the x and y directions. The contrast is assumed constant in the z direction, resulting in a voxel length equal to the thickness of the Mylar sheet (0.12 mm).

The normalized absolute value of the kernel of (8), i.e., the elements of the matrix $\underline{\underline{C}}$, is plotted in Figure 8. Here, the coordinates are given relative to x and y position of the anten-

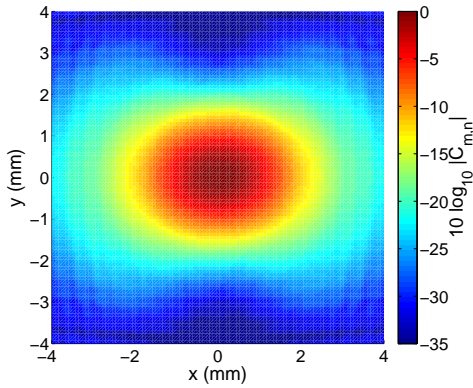


Fig. 8. Normalized amplitude of the elements in $\underline{\underline{C}}$ as a function of x and y relative to the antenna position.

nas and the values are plotted on a dB scale ($10 \log_{10}(C_{m,n})$). From the plot it is seen that the values which are within 3 dB of the maximum values cover an elliptical area of approximately 2 mm by 1 mm in size. Hence, measured signal at any given location contains information about a relatively large area in the imaging domain.

In Figure 9(a), the measured amplitude is plotted as a function of the position of the transmitting antenna. In Figures 9(b) and 9(c), the real and imaginary parts of the contrast in relative permittivity are plotted.

A number of interesting features should be noted in these images. First, in the plot of the measured amplitude, the amplitude of the signal is seen to be approximately 5.7 V when the antennas are placed above the Mylar and approximately 3.5 V along the inside of the edges of the cut-out cross, corresponding to a change in the signal level of 4.2 dB.

This indicates that the scattered field caused by the air in the cut-out cross is not much weaker than the total field, which was assumed during the derivation of the imaging algorithm.

Second, in the plot of the measured amplitude, the highest voltages are measured over the Mylar along the edge of the cut-out cross while the lowest voltages are measured along the edges over the air gap. This is particularly pronounced at the corners of the cut-out cross where the overall maximum amplitudes are measured.

In the processed images, the cross is much more uniform and well-defined than in the plot of the raw amplitude. It is also noted that the contrast is larger in the real part than in the imaginary part. This corresponds well with the fact that both the Mylar sheet and the air in the cut-out cross have almost no loss. Also, it is noted that the real part of the contrast in permittivity in the cross is negative, which corresponds well with the fact that air has a lower permittivity than Mylar. However, a contrast in relative permittivity of approximately -4 is too much since the real contrast is only -1.8 , corresponding to the difference between the relative permittivity of Mylar and air.

This overshoot in contrast is likely a result of the assumption of low-amplitude scattered field not being fulfilled, but discrepancies between the modeled incident fields and the actual incident fields may also be a contributing factor.

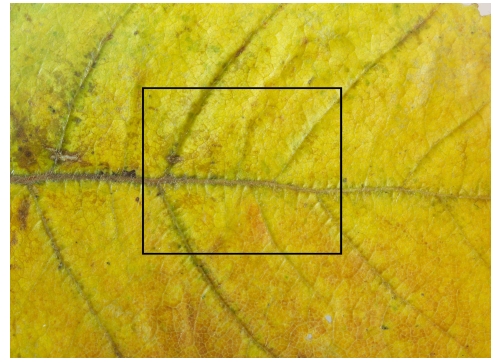


Fig. 10. Photo of the leaf. The black rectangle indicates the imaged area.

It should also be noticed that the effects of the edges observed in the raw data, with high values on the Mylar side and low values on the air side, are not present in the processed images. Here, both the real and imaginary parts of the contrast show a uniform contrast over the Mylar of approximately 0, and a uniform value over the cut-out cross.

The second imaging example, which will be presented in this paper, is an image of a leaf. A photo of the leaf is seen in Figure 10. Leaves have previously been used as test targets for THz imaging and spectroscopy systems by several authors, e.g., [56]–[59]. Leaves generally have a higher water content, and thus absorption, in the veins than in the mesophyll. In Figure 10, the veins are visible as the dark lines while the yellow and brown colors of the mesophyll are due to the fact that the leaf was picked from a tree in the autumn.

The measurement of the leaf was performed by scanning the transmitter and receiver across the sample in steps of 0.2 mm in both the x and y directions. A region of 16 by 16 mm² was imaged and the receiver was kept exactly on the opposite side of the sample from the transmitter. The leaf was positioned between two glass plates, each 0.99 mm thick, and at the center of the imaging domain, the total thickness of the leaf and the two glass plates was measured to be 2.534 mm.

In the model used for calculating the incident fields, the empty system was modeled with two glass plates with a real-valued relative permittivity of 4 on both sides of the imaging domain which was assumed to be 0.554 mm thick and have a background permittivity of 3. A real-valued background permittivity of the imaging domain was chosen because the leaf was picked in the autumn with a relatively dry, and hence low-loss mesophyll.

For the reconstruction of the images, the imaging domain was divided into voxels measuring 0.1 by 0.1 mm² in the xy plane. The contrast was again assumed to be constant in the z direction, yielding a length of the voxels of 0.554 mm.

In Figure 11(a), the measured amplitude is plotted as a function of the position of the transmitting antenna. In Figures 11(b) and 11(c), the real and imaginary parts of the contrast in relative permittivity are shown.

Similar to what was observed for the Mylar target, a significant difference is observed in the measured amplitude for different regions of the image. When the antennas are positioned above the most dry regions of the leaf, the amplitude

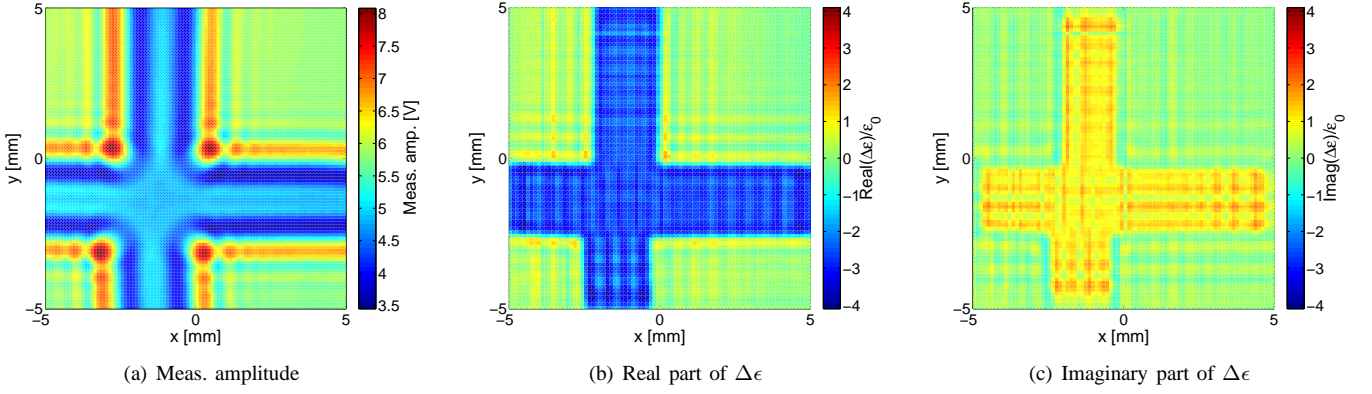


Fig. 9. Images of the Mylar cut-out cross. The measured amplitude (unprocessed data) is shown in (a) and the real and imaginary parts of the contrast in relative permittivity are shown in (b) and (c).

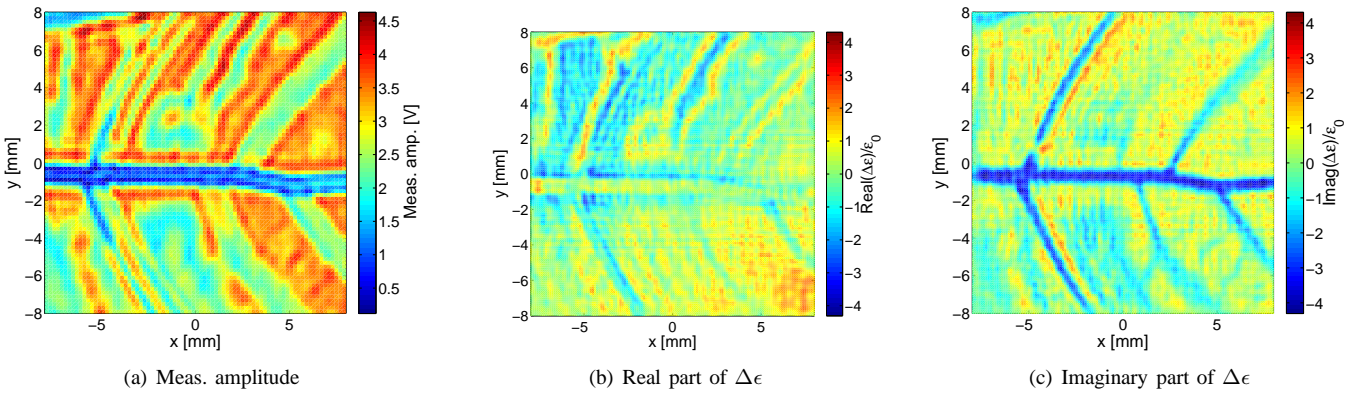


Fig. 11. Images of the leaf. The measured amplitude (unprocessed data) is shown in (a) and the real and imaginary parts of the contrast in relative permittivity are shown in (b) and (c).

is as high as 4.6 V while the amplitude measured when the antennas are positioned above the veins of the leaf is as low as 0.3 V. This corresponds to a change in amplitude of more than 23 dB, indicating that the assumption made in (8) about the total field being approximately equal to the incident field, is not accurate. However, in the processed images shown in Figures 11(b) and 11(c) it is seen that the processed images do indeed show the structures of the leaf. And they also show that the contrast in relative permittivity is dominated by a negative imaginary part along the veins of the leaf. This is to be expected since the water content is higher in the veins than in the mesophyl and a negative contrast in the imaginary part of the permittivity indicates an increase in the loss.

C. General Remarks

In both of the imaging examples presented here, the change in the measured amplitude is so large that the assumption of the total field being equal to the incident field is a poor approximation. However, the processed images are in both cases informative since they show whether the contrast is predominantly in the real or in the imaginary part of the relative permittivity and also show whether this contrast is positive or negative. Hence, although the images are not true quantitative images from which the electromagnetic properties

of the samples can be extracted, they do provide useful information about the contrasts in the samples.

To obtain more accurate estimates of the contrast, work is currently being carried out on improving the accuracy of the computational model used to calculate the incident fields in the imaging domain. This includes both better modeling of the antennas and a more accurate estimate of the permittivity of the glass and permittivity of the background in the imaging domain. Although the Born approximation will still be limiting the ability of the algorithm to reconstruct the true values of high-contrast targets, it is believed that an accurate electromagnetic model will allow for the extraction of the true permittivity values for low-contrast targets, such as cancer samples.

The currently achieved resolution compares well with existing techniques. By introducing multiple voxels in the z-direction and multiple receiver locations for each transmitter location the proposed technique allows for reconstruction of 3D images with the same resolution in both the x-, y- and z-direction.

Since this is an experimental system, partially constructed to test in-house hardware designs, the operating frequency is likely to increase as new hardware for the front-ends is developed. Also, currently the mechanical stage is not optimized for speed. Therefore, a typical measurement containing 10,000

sample points takes approximately one hour. A measurement time of a few minutes or less is realistic with a re-engineered mechanical stage.

VII. CONCLUSION

A THz imaging system operating at 346 GHz has been developed. The system consists of a single transmitter antenna mounted on the opposite side of the sample under investigation from a single receiver antenna. The antennas are mounted on mechanical stages, which allow them to be scanned across the sample.

The antennas used in the system are simple open-ended waveguides. These antennas have a relatively broad beam, resulting in a poor focus in the imaging domain. To remedy this, and to extract more information about the scatterers than what is immediately available from observing the raw measurement data, an imaging algorithm based on the first-order Born approximation has been implemented. This algorithm was shown to improve the resolution of the images as well as provide useful information about the contrast of the samples.

ACKNOWLEDGMENT

The author would like to thank C.M. Kihlman for his work on the high precision machining of the antennas and waveguide blocks.

REFERENCES

- [1] B. Hu and M. Nuss, "Imaging with terahertz waves," *Optics Letters*, vol. 20, no. 16, pp. 1716–1718, 1995.
- [2] W. L. Chan, J. Deibel, and D. M. Mittleman, "Imaging with terahertz radiation," *Reports on Progress in Physics*, vol. 70, no. 8, pp. 1325–1379, Aug. 2007.
- [3] K. B. Cooper, R. J. Dengler, N. Llombart, B. Thomas, G. Chattopadhyay, and P. H. Siegel, "THz Imaging Radar for Standoff Personnel Screening," *IEEE Transactions on Terahertz Science and Technology*, vol. 1, no. 1, pp. 169–182, 2011.
- [4] P. F. Taday, "Applications of terahertz spectroscopy to pharmaceutical sciences," *Philosophical Transactions of the Royal Society A: Mathematical, Physical and Engineering Sciences*, vol. 362, no. 1815, pp. 351–364, Feb. 2004.
- [5] E. Pickwell and V. P. Wallace, "Biomedical applications of terahertz technology," *Journal of Physics D: Applied Physics*, vol. 39, no. 17, pp. R301–R310, Sep. 2006.
- [6] J. W. Waters, L. Froidevaux, R. S. Harwood, R. F. Jarnot, H. M. Pickett, W. G. Read, P. Siegel, R. E. Cofield, M. J. Filipiak, D. A. Flower, J. R. Holden, G. K. Lau, N. J. Livesey, G. L. Manney, H. C. Pumphrey, M. L. Santee, D. L. Wu, D. T. Cuddy, R. R. Lay, M. S. Loo, V. S. Perun, M. J. Schwartz, P. C. Stek, R. P. Thurstans, M. A. Boyles, K. M. Chandra, M. C. Chavez, G.-S. Chen, B. V. Chudasama, R. Dodge, R. A. Fuller, M. A. Girard, J. H. Jiang, Y. Jiang, B. W. Knosp, R. C. LaBelle, J. C. Lam, K. A. Lee, D. Miller, J. E. Oswald, N. C. Patel, D. M. Pukala, O. Quintero, D. M. Scaff, W. Van Snyder, M. C. Tope, P. A. Wagner, and M. J. Walch, "The Earth observing system microwave limb sounder (EOS MLS) on the aura Satellite," *Geoscience and Remote Sensing, IEEE Transactions on*, vol. 44, no. 5, pp. 1075–1092, 2006.
- [7] E. Berry, A. J. Fitzgerald, N. N. Zinov'ev, G. C. Walker, S. Homer-Vanniasinkam, C. D. Sudworth, R. E. Miles, J. M. Chamberlain, and M. A. Smith, "Optical properties of tissue measured using terahertz pulsed imaging," *Proceedings of SPIE: Medical Imaging 2003: Physics of Medical Imaging*, vol. 5030, p. 459470, 2003.
- [8] P. Siegel, "Terahertz technology in biology and medicine," *IEEE Transactions on Microwave Theory and Techniques*, vol. 52, no. 10, pp. 2438–2447, 2004.
- [9] L. Duvillaret, F. Garet, and J. L. Coutaz, "Highly precise determination of optical constants and sample thickness in terahertz time-domain spectroscopy," *Applied Optics*, vol. 38, no. 2, 1999.
- [10] R. Piesiewicz, C. Jansen, S. Wietzke, D. Mittleman, M. Koch, and T. Krner, "Properties of building and plastic materials in the THz range," *International Journal of Infrared and Millimeter Waves*, vol. 28, no. 5, pp. 363–371, Mar. 2007.
- [11] B. Ferguson, S. Wang, D. Gray, D. Abbot, and X. C. Zhang, "T-ray computed tomography," *Optics Letters*, vol. 27, no. 15, p. 13121314, 2002.
- [12] K. W. Kan, W. Lee, W. Cheung, and E. Pickwell-MacPherson, "A pilot study of terahertz pulsed imaging of osteoarthritis," in *33rd International Conference on Infrared, Millimeter and Terahertz Waves, 2008. IRMMW-THz 2008*. IEEE, Sep. 2008, pp. 1–2.
- [13] C. M. Ciesla, D. D. Arnone, A. Corchia, D. A. Crawley, C. Longbottom, E. H. Linfield, and M. Pepper, "Biomedical applications of terahertz pulse imaging," in *Commercial and Biomedical Applications of Ultrafast Lasers II*, J. Neev and M. K. Reed, Eds., vol. 3934. San Jose, CA, USA: SPIE, 2000, pp. 73–81.
- [14] D. A. Crawley, C. Longbottom, B. E. Cole, C. M. Ciesla, D. Arnone, V. P. Wallace, and M. Pepper, "Terahertz pulse imaging: A pilot study of potential applications in dentistry," *Caries Research*, vol. 37, no. 5, pp. 352–359, 2003.
- [15] D. Crawley, C. Longbottom, V. P. Wallace, B. Cole, D. Arnone, and M. Pepper, "Three-dimensional terahertz pulse imaging of dental tissue," *Journal of Biomedical Optics*, vol. 8, no. 2, pp. 303–307, 2003.
- [16] M. Schirmer, M. Fujio, M. Minami, J. Miura, T. Araki, and T. Yasui, "Biomedical applications of a real-time terahertz color scanner," *Biomedical Optics Express*, vol. 1, no. 2, pp. 354–366, 2010.
- [17] T. Löffler, T. Bauer, K. J. Siebert, H. G. Roskos, A. Fitzgerald, and S. Czasch, "Terahertz dark-field imaging of biomedical tissue," *Opt. Express*, vol. 9, no. 12, p. 616621, 2001.
- [18] R. M. Woodward, B. E. Cole, V. P. Wallace, R. J. Pye, D. D. Arnone, E. H. Linfield, and M. Pepper, "Terahertz pulse imaging in reflection geometry of human skin cancer and skin tissue," *Physics in Medicine and Biology*, vol. 47, p. 38533863, 2002.
- [19] E. Pickwell, B. E. Cole, A. J. Fitzgerald, M. Pepper, and V. P. Wallace, "In vivo study of human skin using pulsed terahertz radiation," *Physics in Medicine and Biology*, vol. 49, p. 15951607, 2004.
- [20] V. P. Wallace, A. J. Fitzgerald, E. Pickwell, R. J. Pye, P. F. Taday, N. Flanagan, and T. Ha, "Terahertz pulsed spectroscopy of human basal cell carcinoma," *Applied spectroscopy*, vol. 60, no. 10, p. 11271133, 2006.
- [21] J. Son, "Terahertz electromagnetic interactions with biological matter and their applications," *Journal of Applied Physics*, vol. 105, no. 10, p. 102033, 2009.
- [22] C. Chiu, H. Chen, Y. Huang, W. Lee, Y. Hwang, H. Huang, and C. Sun, "All-terahertz fiber-scanning near-field microscopy," *Optics Letters*, vol. 34, no. 7, pp. 1084–1086, 2009.
- [23] H. Chen, T. Chen, T. Tseng, J. Lu, C. Kuo, S. Fu, W. Lee, Y. Tsai, Y. Huang, E. Y. Chuang, Y. Hwang, and C. Sun, "High-sensitivity in vivo THz transmission imaging of early human breast cancer in a subcutaneous xenograft mouse model," *Optics Express*, vol. 19, no. 22, pp. 21 552–21 562, Oct. 2011.
- [24] H. Chen, W. Lee, H. Huang, C. Chiu, Y. Tsai, T. Tseng, J. Lu, W. Lai, and C. Sun, "Performance of THz fiber-scanning near-field microscopy to diagnose breast tumors," *Optics Express*, vol. 19, no. 20, pp. 19 523–19 531, 2011.
- [25] E. Jung, M. Lim, K. Moon, Y. Do, S. Lee, H. Han, H. Choi, K. Cho, and K. Kim, "Terahertz pulse imaging of micro-metastatic lymph nodes in early-stage cervical cancer patients," *Journal of the Optical Society of Korea*, vol. 15, no. 2, pp. 155–160, Jun. 2011.
- [26] P. Knobloch, C. Schildknecht, T. Kleine-Ostmann, M. Koch, S. Hoffmann, M. Hofmann, E. Rehberg, M. Sperling, K. Donhuijsen, G. Hein *et al.*, "Medical THz imaging: an investigation of histo-pathological samples," *Physics in medicine and biology*, vol. 47, p. 38753884, 2002.
- [27] J. Y. Lu, C. C. Kuo, C. M. Chiu, H. W. Chen, Y. J. Hwang, C. L. Pan, and C. K. Sun, "THz interferometric imaging using subwavelength plastic fiber based THz endoscopes," *Opt. Express*, vol. 16, p. 24942501, 2008.
- [28] M. H. Arbab, T. C. Dickey, D. P. Winebrenner, A. Chen, M. B. Klein, and P. D. Mourad, "Terahertz reflectometry of burn wounds in a rat model," *Biomedical Optics Express*, vol. 2, no. 8, pp. 2339–2347, 2011.
- [29] Z. D. Taylor, R. S. Singh, D. B. Bennett, P. Tewari, C. P. Kealey, N. Bajwa, M. O. Culjat, A. Stojadinovic, H. Lee, J.-P. Hubschman, E. R. Brown, and W. S. Grundfest, "THz Medical Imaging: in vivo Hydration Sensing," *Terahertz Science and Technology, IEEE Transactions on*, vol. 1, no. 1, 2011.
- [30] D. B. Bennett, Z. D. Taylor, P. Tewari, R. S. Singh, M. O. Culjat, W. S. Grundfest, D. J. Sassoon, R. D. Johnson, J. Hubschman, and E. R.

- Brown, "Terahertz sensing in corneal tissues," *Journal of Biomedical Optics*, vol. 16, p. 057003, 2011.
- [31] R. Dahlbäck, T. Rubæk, T. Bryllert, M. Persson, and J. Stake, "A 340 GHz CW non-linear imaging system," in *Infrared Millimeter and Terahertz Waves (IRMMW-THz), 2010 35th International Conference on*, 2010.
- [32] T. Rubæk, R. N. Dahlbäck, A. Fhager, M. Persson, and J. Stake, "A single-channel THz imaging system for biomedical applications," *General Assembly and Scientific Symposium, 2011 XXXth URSI*, 2011.
- [33] T. Rubæk, R. Dahlbäck, A. Fhager, J. Stake, and M. Persson, "A THz imaging system for biomedical applications," in *Antennas and Propagation (EUCAP), Proceedings of the 5th European Conference on*, 2011, pp. 3755–3758.
- [34] W. Chew, *Waves and fields in inhomogeneous media*. New York: IEEE Press, 1995.
- [35] S. Wang and X. C. Zhang, "Pulsed terahertz tomography," *JOURNAL OF PHYSICS-LONDON-D APPLIED PHYSICS*, vol. 37, no. 4, p. 136, 2004.
- [36] D. Mittleman, S. Hunsche, and L. Boivin, "T-ray tomography," *Ultrafast Electronics and Optoelectronics*, vol. 13, 1997.
- [37] H. Kitahara, M. Tani, and M. Hangyo, "Three-Dimensional tomographic imaging in terahertz region," *Japanese Journal of Applied Physics*, vol. 49, no. 2, p. 020207, Feb. 2010.
- [38] B. Ferguson, S. Wang, D. Gray, D. Abbott, and X. Zhang, "Towards functional 3D t-ray imaging," *Physics in Medicine and Biology*, vol. 47, pp. 3735–3742, Nov. 2002.
- [39] X. Zhang, "Three-dimensional terahertz wave imaging," *Philosophical Transactions of the Royal Society of London. Series A: Mathematical, Physical and Engineering Sciences*, vol. 362, no. 1815, pp. 283–299, Feb. 2004.
- [40] V. Krozer, T. Löffler, J. Dall, A. Kusk, F. Eichhorn, R. K. Olsson, J. D. Buron, P. U. Jepsen, V. Zhurbenko, and T. Jensen, "Terahertz imaging systems with aperture synthesis techniques," *IEEE Transactions on Microwave Theory and Techniques*, vol. 58, no. 7, pp. 2027–2039, Jul. 2010.
- [41] T. Hansen and P. Johansen, "Inversion scheme for ground penetrating radar that takes into account the planar air-soil interface," *Geoscience and Remote Sensing, IEEE Transactions on*, vol. 38, no. 1, pp. 496–506, 2000.
- [42] A. Witten, J. Molyneux, and J. Nyquist, "Ground penetrating radar tomography: algorithms and case studies," *Geoscience and Remote Sensing, IEEE Transactions on*, vol. 32, no. 2, pp. 461–467, 1994.
- [43] P. Siegel, "Terahertz heterodyne imaging PART I: introduction and techniques," *International journal of infrared and millimeter waves*, vol. 27, no. 4, pp. 465–480, 2006.
- [44] P. H. Siegel and R. J. Dengler, "Terahertz Heterodyne Imaging Part II: Instruments," *International Journal of Infrared and Millimeter Waves*, vol. 27, no. 5, pp. 631–655, 2007.
- [45] P. J. Sobis, A. Emrich, and J. Stake, "A Low VSWR 2SB Schottky Receiver," *IEEE Transactions on Terahertz Science and Technology*, vol. 1, no. 2, pp. 403–411, 2011.
- [46] J. Doane, "Broadband superheterodyne tracking circuits for millimeter-wave measurements," *Review of Scientific Instruments*, vol. 51, p. 317, 1980.
- [47] K. Cooper, R. Dengler, N. Llobart, T. Bryllert, G. Chattopadhyay, E. Schlecht, J. Gill, C. Lee, A. Skalare, and I. Mehdi, "Penetrating 3-D Imaging at 4- and 25-m Range Using a Submillimeter-Wave Radar," *IEEE Transactions on Microwave Theory and Techniques*, vol. 56, no. 12, Part 1, pp. 2771–2778, 2008.
- [48] C. Am Weg, W. von Spiegel, R. Henneberger, R. Zimmermann, T. Loeffler, and H. Roskos, "Fast Active THz Cameras with Ranging Capabilities," *Journal of Infrared, Millimeter and Terahertz Waves*, vol. 30, no. 12, pp. 1281–1296, 2009.
- [49] T. Bryllert, A. Malko, J. Vukusic, and J. Stake, "A 175 GHz HBV Frequency Quintupler With 60 mW Output Power," *IEEE Microwave and Wireless Components Letters*, vol. 22, pp. 76–78, 2012.
- [50] C.-t. Tai, *Dyadic Green Functions in Electromagnetic Theory*, 2nd ed. Oxford: Oxford University Press, 1995.
- [51] T. Rubk and P. Meincke, "Including antenna models in microwave imaging for breast cancer screening," in *Antennas and Propagation, 2006. EuCAP 2006. First European Conference on*, 2006, p. 16.
- [52] T. Rubk, O. S. Kim, and P. Meincke, "Computational validation of a 3-D microwave imaging system for Breast-Cancer screening," *IEEE Transactions on Antennas and Propagation*, vol. 57, no. 7, pp. 2105–2115, Jul. 2009.
- [53] P. Hansen, *Rank-deficient and discrete ill-posed problems: Numerical aspects of linear inversion*, ser. SIAM monographs on mathematical modeling and computation. Philadelphia: SIAM, 1997.
- [54] S. Krishnamurthy, M. T. Reiten, S. A. Harmon, and R. A. Chevillat, "Characterization of thin polymer films using terahertz time-domain interferometry," *Applied Physics Letters*, vol. 79, no. 6, p. 875, 2001.
- [55] X. Liu, S. MacNaughton, D. B. Shrekenhamer, H. Tao, S. Selvarasah, A. Totachawattana, R. D. Averitt, M. R. Dokmeci, S. Sonkusale, and W. J. Padilla, "Metamaterials on parylene thin film substrates: Design, fabrication, and characterization at terahertz frequency," *Applied Physics Letters*, vol. 96, no. 1, p. 011906, 2010.
- [56] B. B. Hu and M. C. Nuss, "Imaging with terahertz waves," *Optics Letters*, vol. 20, no. 16, pp. 1716–1718, 1995.
- [57] S. Hadjiloucas, L. S. Karatzas, and J. W. Bowen, "Measurements of leaf water content using terahertz radiation," *IEEE Transactions on Microwave Theory and Techniques*, vol. 47, no. 2, pp. 142–149, Feb. 1999.
- [58] B. Ferguson and D. Abbott, "De-noising techniques for terahertz responses of biological samples," *Microelectronics Journal*, vol. 32, no. 12, pp. 943–953, Dec. 2001.
- [59] C. Jrdens, M. Scheller, B. Breitenstein, D. Selmar, and M. Koch, "Evaluation of leaf water status by means of permittivity at terahertz frequencies," *Journal of Biological Physics*, vol. 35, pp. 255–264, Jun. 2009.



Robin Dahlbäck (S10) received the M.Sc.E.E degree from Chalmers University of Technology, Göteborg, Sweden, in 2010, and is currently working towards the Ph.D. degree from the Terahertz and Millimetre Wave Laboratory, Chalmers University of Technology. His research topics include THz imaging, system design and high power THz solid state sources.



Tonny Rubæk received the M.Sc.E.E. and PhD degrees from the Technical University of Denmark in 2004 and 2008, respectively. His research interests include electromagnetic imaging algorithms and hardware.



Mikael Persson (M10) received the M.Sc. and Ph.D. degrees from Chalmers University of Technology, Göteborg, Sweden, in 1982 and 1987, respectively. In 2000, he became a Professor of electromagnetics and in 2006 a professor in biomedical electromagnetics at the Department of Signal and Systems, Chalmers University of Technology. He is presently the Head of the Division of Signal Processing and Biomedical Engineering and the Director for the regional research and development platform MedTech West. At present these activities involve approximately 50 researchers. His main research interests include electromagnetic diagnostics and treatment. He is author/coauthor of more than 200 refereed journal and conference papers



Jan Stake (S95M00SM06) was born in Uddevalla, Sweden in 1971. He received the degrees of M.Sc. in electrical engineering and Ph.D. in microwave electronics from Chalmers University of Technology, Göteborg, Sweden in 1994 and 1999, respectively.

In 1997 he was a Research Assistant at the University of Virginia, Charlottesville, USA. From 1999 to 2001, he was a Research Fellow in the millimetre wave group at the Rutherford Appleton Laboratory, UK. He then joined Saab Combitech Systems AB as a Senior RF/microwave Engineer until 2003. From 2000 to 2006, he held different academic positions at Chalmers and was also Head of the Nanofabrication Laboratory at MC2 between 2003 and 2006. During the summer 2007, he was a Visiting Professor in the Submillimeter Wave Advanced Technology (SWAT) group at Caltech/JPL, Pasadena, USA. He is currently Professor and Head of the Terahertz and Millimetre Wave Laboratory at the department of Microtechnology and Nanoscience (MC2), Chalmers, Göteborg, Sweden. His research involves sources and detectors for terahertz frequencies, high frequency semiconductor devices, graphene electronics, terahertz measurement techniques and applications. He is also co-founder of Wasa Millimeter Wave AB.

Prof. Stake serves as Topical Editor for the IEEE Transactions on Terahertz Science and Technology.